SPECIAL
Air-sea interaction during PISTON-MISOBOB-CAMP2Ex
COLLECTION

Longwave Radiation Corrections for the OMNI Buoy Network

K. JOSSIA JOSEPH,[a] AMIT TANDON,[b] R. VENKATESAN,[a] J. THOMAS FARRAR,[c] AND ROBERT A. WELLER[c]

[a] *National Institute of Ocean Technology, Ministry of Earth Sciences, Chennai, India*
[b] *University of Massachusetts Dartmouth, North Dartmouth, Massachusetts*
[c] *Woods Hole Oceanographic Institution, Woods Hole, Massachusetts*

(Manuscript received 23 May 2021, in final form 8 October 2021)

ABSTRACT: The inception of a moored buoy network in the northern Indian Ocean in 1997 paved the way for systematic collection of long-term time series observations of meteorological and oceanographic parameters. This buoy network was revamped in 2011 with Ocean Moored buoy Network for north Indian Ocean (OMNI) buoys fitted with additional sensors to better quantify the air–sea fluxes. An intercomparison of OMNI buoy measurements with the nearby Woods Hole Oceanographic Institution (WHOI) mooring during the year 2015 revealed an overestimation of downwelling longwave radiation (LWR↓). Analysis of the OMNI and WHOI radiation sensors at a test station at National Institute of Ocean Technology (NIOT) during 2019 revealed that the accurate and stable amplification of the thermopile voltage records along with the customized datalogger in the WHOI system results in better estimations of LWR↓. The offset in NIOT measured LWR↓ is estimated first by segregating the LWR↓ during clear-sky conditions identified using the downwelling shortwave radiation measurements from the same test station, and second, finding the offset by taking the difference with expected theoretical clear-sky LWR↓. The corrected LWR↓ exhibited good agreement with that of collocated WHOI measurements, with a correlation of 0.93. This method is applied to the OMNI field measurements and again compared with the nearby WHOI mooring measurements, exhibiting a better correlation of 0.95. This work has led to the revamping of radiation measurements in OMNI buoys and provides a reliable method to correct past measurements and improve estimation of air–sea fluxes in the Indian Ocean.

SIGNIFICANCE STATEMENT: Downwelling longwave radiation (LWR↓) is an important climate variable for calculating air–sea heat exchange and quantifying Earth's energy budget. An intercomparison of LWR↓ measurements between ocean observing platforms in the north Indian Ocean revealed a systematic offset in National Institute of Ocean Technology (NIOT) Ocean Moored buoy Network for north Indian Ocean (OMNI) buoys. The observed offset limited our capability to accurately estimate air–sea fluxes in the Indian Ocean. The sensor measurements were compared with a standard reference system, which revealed problems in thermopile amplifier as the root cause of the offset. This work led to the development of a reliable method to correct the offset in LWR↓ and revamping of radiation measurements in NIOT-OMNI buoys. The correction is being applied to the past measurements from 12 OMNI buoys over 8 years to improve the estimation of air–sea fluxes in the Indian Ocean.

KEYWORDS: Algorithms; Buoy observations; In situ oceanic observations; Instrumentation/sensors; Quality assurance/control

1. Introduction

The downwelling longwave radiation (LWR↓) is an important component of the air–sea flux studies, and radiative energy budget. The LWR↓ exhibits significant variability due to clouds and greenhouse effect, which is utilized in cloud detection studies, identification of clear-sky conditions, and climate change studies (Philipona et al. 1996; Ohmura et al. 1998; Marty 2000; Marty and Philipona 2000; Philipona et al. 2001). Attempts are made to estimate the radiative fluxes from satellite observations but with coarse spectral and spatial resolution (Pinker et al. 2014; Tomita and Kubota 2004). The most widely used method for estimating radiative fluxes over the global scale is based on the International Satellite Cloud Cover Project (Rossow and Schiffer 1999). The radiative fluxes derived from MODIS observations of *Terra* and *Aqua* satellites provided comparatively higher spatial resolution as good as 250 m and global coverage every 1–2 days (King et al. 1992; Pinker et al. 2009; Venugopal et al. 2016; Ramesh Kumar et al. 2017). The earlier studies of surface heat flux in the Indian Ocean addressed by Hastenrath and Lamb (1979) and Jones et al. (1995) used monthly mean values, which could not address frequencies higher than seasonal variability.

Denotes content that is immediately available upon publication as open access.

Corresponding author: Amit Tandon, atandon@umassd.edu

Publisher's Note: This article was revised on 23 March 2022 to designate it as open access.

DOI: 10.1175/JTECH-D-21-0069.1

Tomita and Kubota (2004) analyzed the heat flux variability and the relative importance of its different components using the ship-based COADS dataset in the Indian Ocean and emphasized the importance of accurate measurements in assessing the higher frequency variability of flux terms. Computation of radiative fluxes depends partly on the vertical distribution of gaseous absorbers, clouds, and temperature with water vapor alone accounting for 60% of the clear sky (Kiehl and Trenberth 1997). In the tropics, clouds and deep convection (e.g., Rajeevan et al. 2013) are other important factors in modulating the radiative forcing.

LWR↓ exhibits significant variability over different time scales. There are few in situ records that can quantify this variability in the marine environment, so most studies have needed to rely on LWR↓ products that lack realistic high-frequency variability. Pinker et al. (2018) reported good agreement between MODIS satellite derived LWR↓ with that of moored buoy measurements in southeastern Pacific Ocean during the period 2000–12. Thandlam and Rahaman (2019) analyzed various LWR↓ data products during the period 2001–09 and reported an overestimation of LWR↓ in satellite data and hybrid products with the highest error in Indian Ocean region. The uncertainties in deriving the longwave radiation make it difficult to accurately estimate the radiative energy balance, one of the largest uncertainties in global climate change research (Ramanathan et al. 1989). While various observational programs in Pacific and Atlantic Oceans provided insight into the variability of air–sea fluxes in those regions (Fairall et al. 1996; Weller and Anderson 1996; Zeng et al. 1998; Webster et al. 2002). The Indian Ocean remained undersampled until the establishment of India's moored buoy program except for a few process studies such as 1977 Monsoon Experiment (MONEX-77), Indian Ocean Experiment (INDOEX) during 1990s, Bay of Bengal Monsoon Experiment (BOBMEX) in 1999, and Arabian Sea Monsoon Experiment (ARMEX) during 2002/03. The detailed analysis of the fluxes from these process observations (Bhat et al. 2000, 2001; Kumar et al. 2001; Bhat and Chandrasekhar 2001; Bhat 2003; Sengupta et al. 2008; Foltz et al. 2010; McPhaden and Foltz 2013) provided firsthand information about the distinctive variability of meteorological and oceanographic parameters in the Indian Ocean and reported significant variability in net heat flux during the monsoon season.

The systematic measurement and real-time transmission of met-ocean parameters from strategic locations in Indian Seas was initiated with the establishment of moored buoy network by National Institute of Ocean Technology (NIOT) under the aegis of the Ministry of Earth Sciences (erstwhile Department of Ocean Development), Government of India, in 1997 (Premkumar et al. 2000). This network enabled the estimation of turbulent heat fluxes, but was missing radiative fluxes. The introduction of Ocean Moored buoy Network for north Indian Ocean (OMNI) buoys in 2009 with radiation sensors and other additional sensors (Venkatesan et al. 2013) provided the capability to quantify the heat budget at many sites in the northern Indian Ocean (Fig. 1).

NIOT maintains two OMNI moorings in the northern Bay of Bengal (BoB) to analyze the pathways of freshwater influx and its role in monsoon dynamics. As part of an India–U.S.

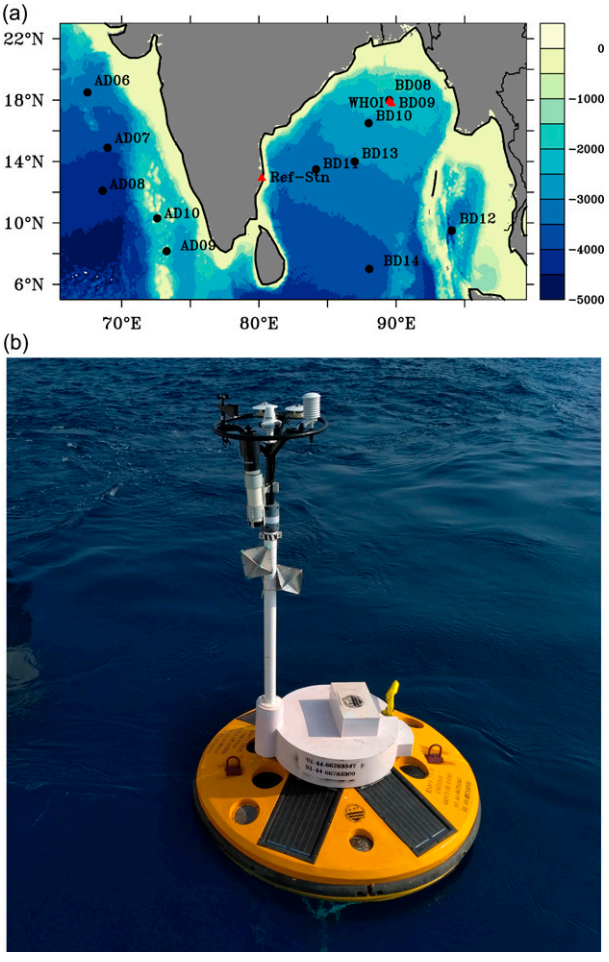

FIG. 1. (a) Location map of OMNI buoys along with test station at NIOT and WHOI buoy and (b) moored data buoy.

collaboration, Woods Hole Oceanographic Institution (WHOI) deployed a mooring (18°N, 89.75°E) in northern BoB close to the NIOT-OMNI BD09 mooring (17.8°N, 89.87°E) which carried out measurements from 8 December 2014 to 29 January 2016. In general, the intercomparison of BD09 and WHOI mooring meteorological parameters showed excellent correlation. However, the LWR↓ values from BD09 were overestimated. A preliminary analysis pointed toward an issue with the amplifier used in NIOT-OMNI buoys (which amplifies thermopile voltages from microvolts to millivolts), compared to that of the amplification and signal processing electronics used by WHOI in measuring LWR↓.

To investigate this issue in detail, a test station was installed at NIOT to evaluate and compare sensor performance and data processing. The test station used three different dataloggers: the General Interface (GENI) logger used on NIOT-OMNI buoys (hereafter NIOT-OMNI), the WHOI Air–Sea interaction Improved Meteorological (ASIMET) datalogger, and a Campbell datalogger. The dataloggers were each connected to calibrated Eppley radiometers, which were installed side by side to intercompare the sensor-logger performance (Fig. 2). The Campbell and

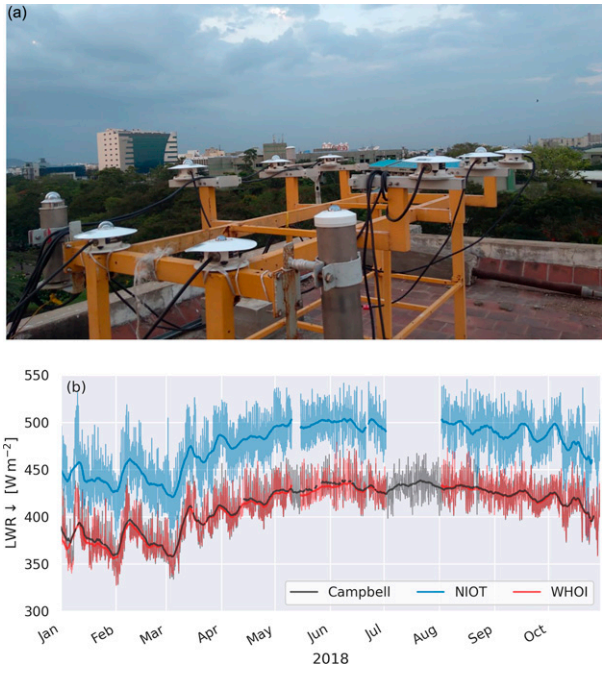

FIG. 2. (a) The collocated radiation sensors (NIOT-OMNI, WHOI, and Campbell) and (b) the time series measurements of LWR↓ from them at the NIOT test station during 2018. The thin lines represent the hourly measurements whereas the corresponding thick lines represent the weekly moving averages.

WHOI LWR↓ measurements are in good agreement with a correlation of 0.94 and an RMS error of 9.60 W m^{-2}, whereas that of NIOT-OMNI setup at the test station exhibited an overestimation of 67.34 W m^{-2} compared to that of WHOI with a correlation of 0.88 and an RMS error of 68.96 W m^{-2}.

The huge volume of LWR↓ measurements from 12 OMNI buoys during the period 2011–18 necessitated development of a method to correct the offset and motivated the present study. The offset of the NIOT LWR↓ varies with each deployment, ruling out the possibility of identifying a uniform offset value to correct the past measurements.

Here we present an approach to apply a correction to each NIOT LWR↓ data record. In broad terms, the approach is to identify clear-sky conditions using other measurements (downwelling solar radiation) and to then use the theoretical clear-sky LWR↓ to estimate a correction for the OMNI-NIOT setup. Detailed analysis revealed that the overestimation in the NIOT LWR↓ measurements is likely due to the issues with amplifiers. It also suggested that WHOI system has the advantage of placing the amplification, signal processing and digitization electronics close to the sensor. This study explains the background, experimental setup, the intercomparison results, the offset correction at the test station, and the extension of the method for correcting the field observations.

2. Data and methods

The systematic measurement of radiative fluxes in the BoB and the Arabian Sea started with the establishment of OMNI buoys, in the year 2010, which was first of its kind in the Indian moored buoy network. These moorings were fitted with Precision Infrared Radiometer (PIR) for LWR↓ and Precision Spectral Pyranometer (PSP) for downwelling shortwave radiation (SWR↓), both from the Eppley Laboratory, Inc.

a. Instrumentation

The pyrgeometer is the standard instrument used to measure the LWR↓. The PIR developed by Eppley Laboratory in Newport, Rhode Island, has been widely used ever since its introduction in 1970. The Eppley PIR has undergone several revisions based on the review and feedback from several investigators (Enz et al. 1975; Albrecht and Cox 1977; Fairall et al. 1996; Philipona et al. 1995; Payne and Anderson 1999; Philipona et al. 2001) such as correction for the dome heating effect. The PIR consists of a blackened disk mounted under a silicon dome with an interference coating on the inside. The disk sits on top at the top end of a thermopile, the other end of which is in thermal contact with the instrument body. The thermopile detector measures the "net radiation" of the PIR, including the downwelling longwave from the sky and longwave from the nearby components of the sensor. The case thermistor is used to determine the outgoing radiation from the case and dome thermistor measures the dome temperature. To shield the blackened disk and thermopile from shortwave radiation, Eppley uses a silicon hemisphere with a vacuum deposited filter on the inside dome (PIR user manual; EPLAB 2016). The transmittance of this dome resembles that of silicon with a sharp lower cut-on between 3.5 and 4 μm, which is the dome constant k in Eq. (1).

Surface radiation measurements in the marine environment have faced many challenges and significant efforts have been made to reduce the uncertainties and to ensure the reliability of LWR↓ measurement. Dickey et al. (1994) suggested hybrid measurement and improvement in calibration procedures to achieve a targeted error limit of 10 W m^{-2} for the monthly mean net longwave heat flux. Payne and Anderson (1999) reported poor adaptation of Eppley PIR in marine environment due to galvanic corrosion and damage to fragile radiation shield. Philipona et al. (1998, 2001) carried out a detailed study with more than 15 collocated pyrgeometers, which depicted a very good agreement of $<$2 W m^{-2}. The persistent efforts of the Upper Ocean Process group at WHOI resulted in significant improvement in LWR↓ measurements with the ASIMET longwave (Hosom et al. 1995) sensor module with improved accuracy and reduced errors, which is presented in detail in section 2c.

PRECISION INFRARED RADIOMETER

The PIR provides the thermopile output in μV, which has a very small full-scale output range (less than 1.5 mV). This signal is amplified using a gain stage amplifier and digitized using an analog-to-digital (AD) converter. The thermopile measurements are corrected for the temperature effects using the case temperature. The dome temperature is an optional correction to the final result to compensate for the dome heating effect. The formula presented by Albrecht and Cox (1977) is used to compute the LWR↓:

TABLE 1. Specifications of the PIR sensor.

Application	Working standard or network measurements
Traceability	World Infrared Standard Group (WISG) and International Practical Temperature Scale (IPTS)
Field of view	180° (2π sr)
Spectral range	~4–50 μm
Sensitivity	~3 μV (W m^{-2})$^{-1}$
Impedance	~700 Ω
Operating temperature	−50° to +80°C
Temperature response	0.5% (−30° to +50°C)
95% response time	5 s
Stability	1% yr^{-1}
Linearity	0.5%
Zero offset	2 W m^{-2}
Uncertainty	5 W m^{-2}

TABLE 2. Specifications of the NIOT-OMNI data acquisition unit: GENI.

OS	Standard real-time operating system (Linux)
Interfaces	Analog, digital, frequency, RS232, RS422/485, relay contacts, power control, etc.
Processor	PXA255 XScale RISC processor running at 400 MHz
Precise RTC	Accurate to ±1 min month^{-1}
Program memory	32-MB flash
SDRAM	64 MB
Data memory	512-MB flash (or more)
Analog input	
Resolution	16 bit
Range	±5 V

$$R_{\text{in}} = \frac{V_{\text{ac}}}{S} + \sigma T_c^4 - k\sigma\left(T_d^4 - T_c^4\right), \tag{1}$$

where V_{ac} is the thermopile measurement output (μV), S is the PIR sensitivity, T_c is the case temperature, T_d is the dome temperature, σ is the Stefan–Boltzmann constant (5.6697×10^{-8} W m^{-2} K^4), and k is a constant. The thermopile sensitivity is given in units of μV W^{-1} m^2 for PIR calibration and the dome constant k varies between 3.5 and 4.

b. NIOT-OMNI system for LWR↓ measurement

The NIOT-OMNI buoy utilizes the data acquisition unit GENI, from Fugro OCEANOR, for data acquisition, data analysis, data storage, and transmission. The processing of LWR↓ and SWR↓ sensor data is carried out by GENI. The system has high processing capability with low power consumption, which runs on standard real-time Linux operating system. GENI is equipped with flexible interfaces for direct connection to a variety of different sensors. All inputs/outputs are electromagnetic interference (EMI) filtered and electrostatic discharge (ESD) protected (Wavescan Buoy; Fugro OCEANOR 2012). The GENI provides 16-bit resolution and ±5-V range for analog inputs such as PIR. The PIR sensor has a very small full-scale output range, less than 1.5 mV, and hence it is connected to the AD converter through a gain amplifier supplied by Fugro OCEANOR. The PIR sensor is calibrated by Eppley before the deployment. See Table 1 for the PIR sensor specifications and Table 2 for GENI specifications.

c. WHOI ASIMET system

The Upper Ocean Process Group at WHOI has carried out extensive efforts to test, evaluate, and develop meteorological sensors and specific electronics for unattended use on ships and buoys (Hosom et al. 1995). The team faced many challenges particularly in achieving the desired accuracy in LWR↓ measurements. Extensive laboratory and field tests led to the development of Improved Meteorological (IMET) system and later developed the advanced module ASIMET system, an intelligent sensor module with all sensor-specific functions such as signal conditioning, data conversion, calibration, processing algorithms, formatting for recording, and network communications along with the sensors (Weller et al. 2012; Weller 2018). In the longwave module the amplifier and AD conversion electronics are placed close to the PIR to reduce possible noise from interference and a very stable amplifier that maintains both offset and gain is used. A series of procedures are performed before, during, and after deployment to ensure high-quality meteorological data.

WHOI has incorporated in their design a modified sensor housing for the Eppley PIR and calibrate each longwave sensor before and after the deployment using a blackbody cavity in a water bath (Payne and Anderson 1999). Module electronics are calibrated separately using high-accuracy voltage and resistance standards. Module measurements for both are then compared with an Eppley PSP and Kipp and Zonen Pyrgeometer CG-4 secondary standards calibrated by the National Renewable Energy Laboratory (NREL) using a rooftop test facility and the module constants are adjusted to agree with the secondary standards (Weller 2006, 2018).

The Eppley PIR integrated in the ASIMET system is set up as a module that stores calibration information and module identification information. Downwelling longwave is computed in the module using sensor outputs sampled once a minute. The module records the sensor outputs and the computed LWR↓ internally at an interval of 1 min and also sends these to the buoy CPU. The module can be used as a standalone unit, or it can be linked to a central datalogger (Fig. 3). Development of a stable and accurate amplifier that maintained gain and offset when powered down and powered up, calibration of the module electronics with known voltage inputs, checking the longwave with blackbody water bath, and comparisons with a secondary standard have considerably reduced the errors to less than 4 W m^{-2} (Weller 2018; Weller et al. 2020). Recording of both the computed downwelling longwave and the raw sensor outputs has proven useful in analyzing module performance.

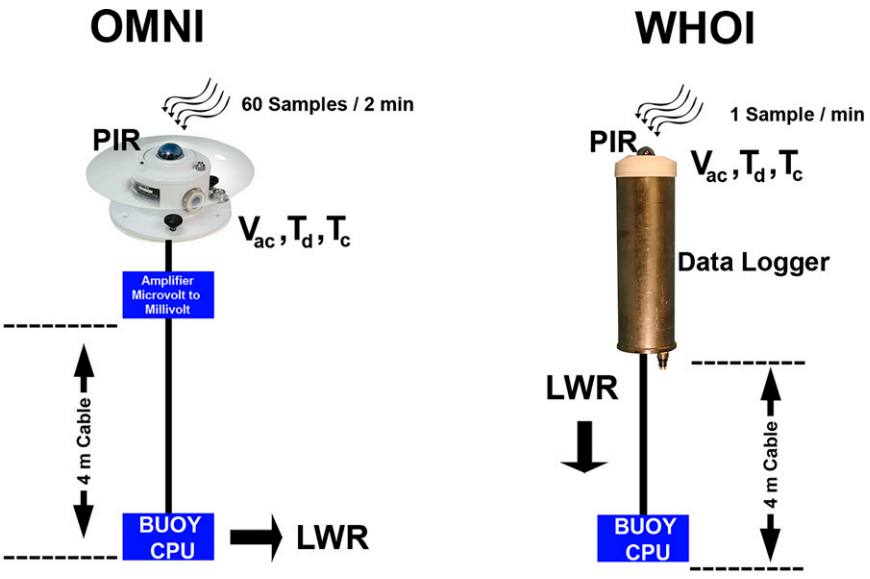

FIG. 3. A schematic showing the NIOT-OMNI and the WHOI LWR↓ measurement systems.

d. *Quality control of LWR↓ measurements*

The analysis revealed large spikes in NIOT LWR↓, particularly in the field measurements, which were due to the zero-volt or the sudden fluctuations of the amplified thermopile output. The zero values are replaced by the nearest preceding/succeeding nonzero value from the high-frequency measurements at 2-min intervals. Similarly, deviation of more than 5% from the 13-h moving-average value is considered as a spike and is replaced with the nearest value with least deviation from the 10-min window of the high-frequency measurements.

e. *Computation of clear-sky radiance*

Clear-sky fluxes are utilized as a tuning parameter in numerical models and also indicate seasonal and regional variability of fluxes. The clear-sky LWR↓ ($\mathrm{LWR}\downarrow_{\mathrm{cl}}$) varies with latitude and depends on the specific humidity and air temperature:

$$\mathrm{LWR}\downarrow_{\mathrm{cl}} = \varepsilon_{e0}\sigma T_a^4, \tag{2}$$

where ε_{e0} is the effective emissivity for clear sky and σ is the Stefan–Boltzmann constant and T_a is air temperature. Fairall et al. (2008) modified the Brunt (1932) formulation for estimating ε_{e0} by adding the total integrated column water vapor (IV) for a three-parameter fit:

$$\varepsilon_{e0} = A + B\sqrt{q_a} - 0.0188 - 0.0063\,\mathrm{IV}, \tag{3}$$

where q_a is specific humidity in g kg^{-1}, whereas IV was obtained through retrieval of surface-based microwave radiance measurements. The coefficients A and B are estimated using the data from Pan American Climate Studies (PACS) cruises within 15° of the equator in eastern Pacific Ocean (Fairall et al. 2008):

$$A = 0.50 + \frac{0.13}{60}\mathrm{abs(lat)}, \tag{4}$$

$$B = 0.091 - \frac{0.03}{60}\mathrm{abs(lat)}, \tag{5}$$

where "lat" is the latitude in degrees.

The clear-sky SWR↓ ($\mathrm{SWR}\downarrow_{\mathrm{cl}}$) is estimated using the parameterization of solar radiation in Iqbal (1988) using the solar constant 1367 W m^{-2} (Fairall et al. 2008). The direct and diffuse solar irradiance are estimated using atmospheric pressure, specific humidity, and coefficients such as integrated water vapor, aerosol absorption coefficients and ozone thickness along with the location details and time of the day, which resembles a smooth bell curve.

f. *NGFS reanalysis data*

The National Centre for Medium Range Weather Forecasting (NCMRWF) provides weather forecasts in real time using the advanced numerical weather prediction system NCMRWF Global Forecast System (NGFS) since 1994. The dataset is upgraded to a horizontal resolution of about 22 km with 64 levels utilizing most of the available meteorological and oceanographic satellite datasets apart from the measured datasets (Prasad et al. 2011, 2017). The dataset is further improved using 3D Var assimilation system and generated a 20-yr retrospective analysis (NGFS Reanalysis) for the period 1999–2018. The 6-hourly total precipitable water from NGFS available at 25-km grid size is utilized to estimate the effective emissivity for clear sky. A comparison of this dataset with the total column water vapor of ERA-Interim exhibited a correlation of 0.98.

g. Segregation of clear-sky LWR↓

Identification of the clear-sky measurements is a major step in this study, which is achieved by utilizing the collocated SWR↓ measurements. We use the daily peak values of measured SWR↓ for identifying the clear-sky conditions and note that the peak occurs at 0600 UTC (1130 Indian standard time, IST) at the test station every day. These values are compared with the estimated theoretical values of $SWR\downarrow_{cl}$ [Eq. (2)] and are qualified as clear sky when the difference is less than 5% of the corresponding $SWR\downarrow_{cl}$.

The measured LWR↓ values corresponding to the clear-sky values of SWR↓ are segregated and the outliers with more than 3 times the standard deviation (3σ) are removed. The offset in LWR↓ is estimated by comparing the clear-sky values of measured LWR↓ with that of the estimated $LWR\downarrow_{cl}$ and the average offset between these values is utilized to correct the LWR↓ measurements at the test station. The same clear-sky method is then applied to correct the field measurement in north BoB during the year 2015, and then evaluated against the WHOI mooring.

3. Development of the algorithm

a. Weather during the study period

The test station is set up on top of the tallest building in NIOT campus in a shadow free, obstacle free area and measurements were made continuously from January 2018 to March 2019. The PIRs are placed on the rooftop to avoid any obstructions (artificial and natural) and shadows (Fig. 2a). Detailed analysis of the data is carried out using the data from January and February 2019, which represents the end of the winter season and is generally fair weather with mostly clear sky (Weller et al. 2019), and hence provides a suitable condition to compare clear-sky conditions. The test station is located at 5.5 km from the west coast of the BoB and is close to the Pallikaranai marshland in Chennai, which also ensures an appropriate ambience for the test station.

The air temperature, relative humidity, and wind exhibit significant diurnal variability whereas that of air pressure exhibits semidiurnal variability (Fig. 4). The wind direction in the beginning is predominantly northerly, which gradually changes to northeasterly. The direction varies between north-northeasterly and north-northwesterly indicating the effect of land–sea breezes. The wind speeds are generally low, with a maximum of 4.38 m s^{-1}, peaking in the afternoon hours during the sea breeze and close to zero in early morning hours during the land breeze.

The air temperature indicates a cool period which varies between 19.82° and 30.87°C with an average diurnal amplitude of 5.3°C. The air temperature was nearly steady for the first half of the observational period, which shows an increasing trend with lesser diurnal amplitude and the predominance of northeasterly winds. Air pressure exhibits semidiurnal viability which varies between 1006.84 and 1018.04 hPa with an average of 1013.03 hPa. The relative humidity exhibits large amplitude diurnal variability of more than 30% for most of the days with

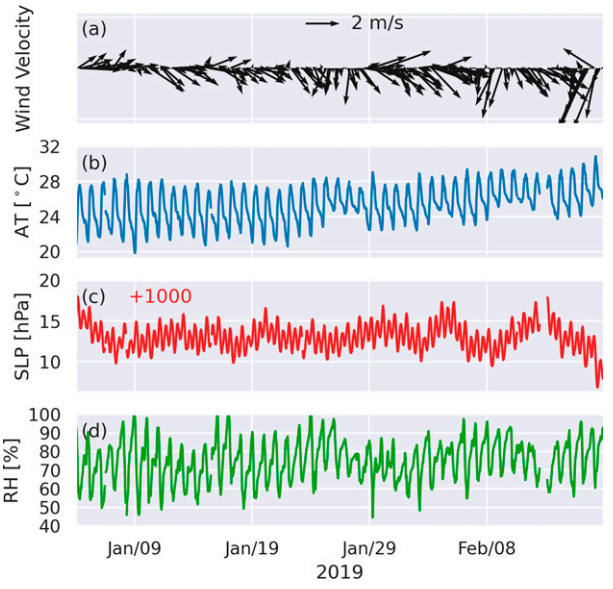

FIG. 4. Time series observations of (a) wind, (b) air temperature, (c) sea level pressure, and (d) relative humidity during the study period.

an average of 74.97%, which ranges between 44.53% and 99.84% (Table 3). A slowly increasing trend with predominance of northeasterly winds is observed in relative humidity.

b. Root-cause analysis

The time series of the individual components of the PIR sensor (case temperature, dome temperature, and thermopile voltage) from collocated WHOI and NIOT PIR sensors were analyzed in detail during the period 4 January–17 February 2019. All three parameters exhibited an increasing trend with significant diurnal variability. The case temperature and dome temperature recorded the minimum during the early morning hours and reached its peak during midday, whereas the thermopile voltage reached its peak during the early morning hours and recorded the minimum during midday.

The intercomparison of case temperature and dome temperature showed good correlation, which reveals the reliability of thermistor measurements (Fig. 5). However, the differences in peak and trough are observed wherein WHOI observations are higher than that of NIOT at the peaks and lower than that of NIOT at the troughs, possibly due to transmission losses. The dome temperature comparison also exhibits similar results. The WHOI (NIOT) measurements exhibit

TABLE 3. Statistics of surface meteorological observations.

Parameter	Mean	Min	Max	Std dev	Std error
Wind speed (m s^{-1})	0.96	0.00	4.38	0.91	0.03
Air temperature (°C)	25.34	19.82	30.87	2.05	0.06
Air pressure (hPa)	1013.03	1006.84	1018.04	1.65	0.05
Relative humidity (%)	74.97	44.53	99.84	11.01	0.34

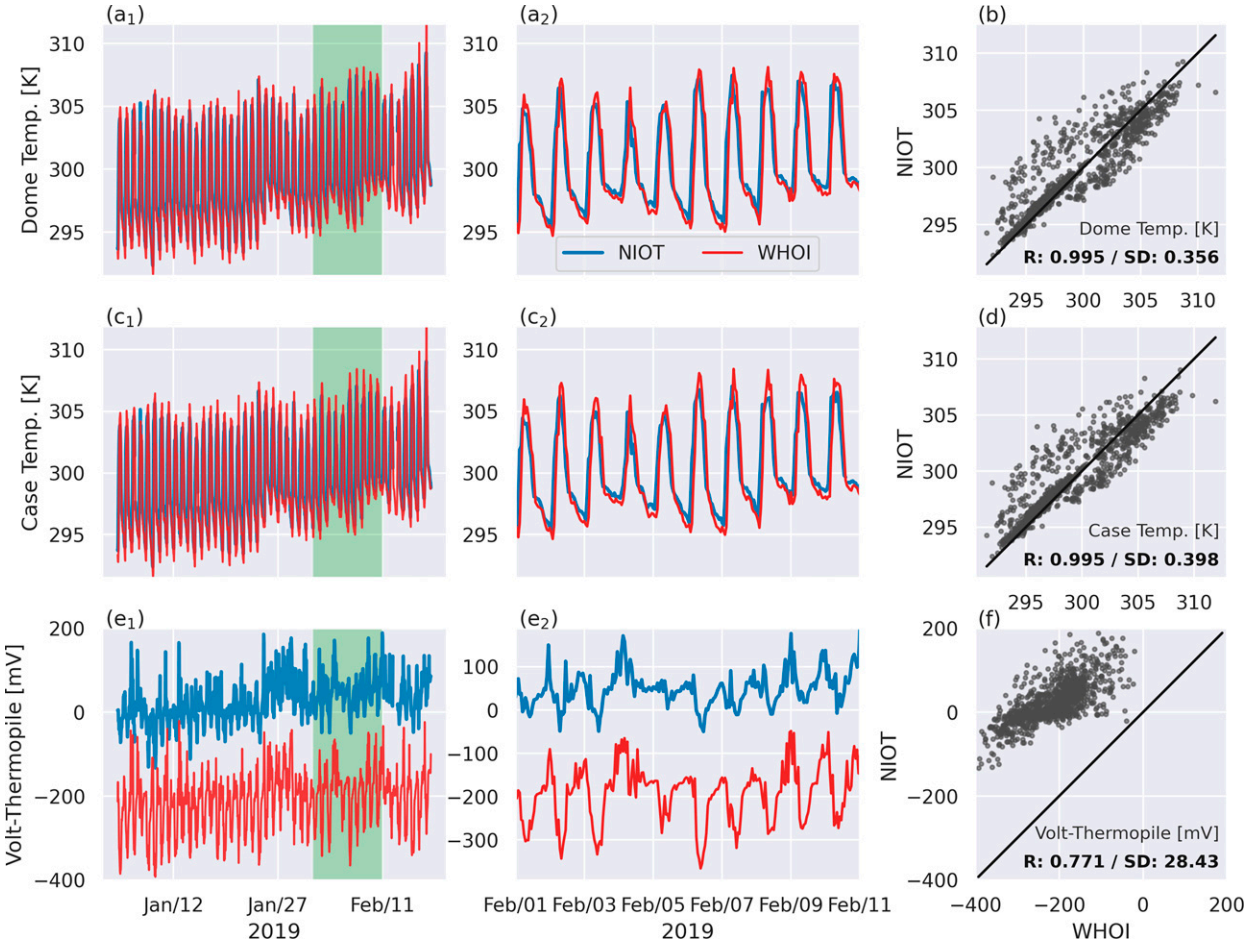

FIG. 5. Time series and regression plots of (a),(b) dome temperature, (c),(d) case temperature, and (e),(f) thermopile volt; (a2),(c2),(e2) Enhanced view of the highlighted portions of (a1), (c1), and (e1), respectively.

comparatively larger (smaller) diurnal amplitudes of 10.91 (9.35) K in case temperature and 10.73 (9.01) K in dome temperature. The case temperature and dome temperature exhibited a correlation of 0.99 with a standard deviation of 0.54 and 0.59 K, respectively.

The intercomparison of thermopile voltage exhibited a clear offset with that of WHOI measurement indicating the reason for the observed offset in LWR↓ measurements. It is observed that NIOT measurements include both positive and negative values whereas that of WHOI remains negative. Moreover, the diurnal amplitude for the NIOT setup is 123.58 mV, much smaller than that of 211.16 mV, the corresponding WHOI setup amplitude. The WHOI measurements exhibit sudden rise and fall with clustered measurements close to the peak and trough similar to that of case temperature and dome temperature measurements. Gradual rise and fall are observed in NIOT measurements except for a few peaks and troughs which are also evident in the comparatively large scatter in the regression plot. The different responses resulted in lower correlation of 0.76 and a standard deviation of 31.13 mV with large offset of 139.43 mV.

An analysis of the voltage measurements in NIOT at 1-h intervals revealed a few zero values preceded and succeeded by nonzero values. These zero values were replaced by the average of the preceding and succeeding nonzero values from the high-frequency dataset recorded at every 2-min interval. In this study, three such observations are replaced. The high-frequency dataset is further examined carefully and has a few spikes, which coincided with the hourly measurements as sudden peaks or lows. These spikes are also replaced with the average of the preceding and succeeding values recorded at 2-min interval. These quality control measures significantly improved the correlation with WHOI volt measurements and recomputed corresponding LWR↓ values.

The analysis clearly points to error in the amplified signal in the thermopile measurements of the NIOT sensor stemming from malfunctioning of the gain amplifier leading to an offset. The errors in measurement (frequent power on/off, lesser wait time before sampling, and sensor self-heating), and radio frequency interference with low-level analog signals could also have contributed apart from the issues with the gain amplifier. The actual sensor measurement in μV, which

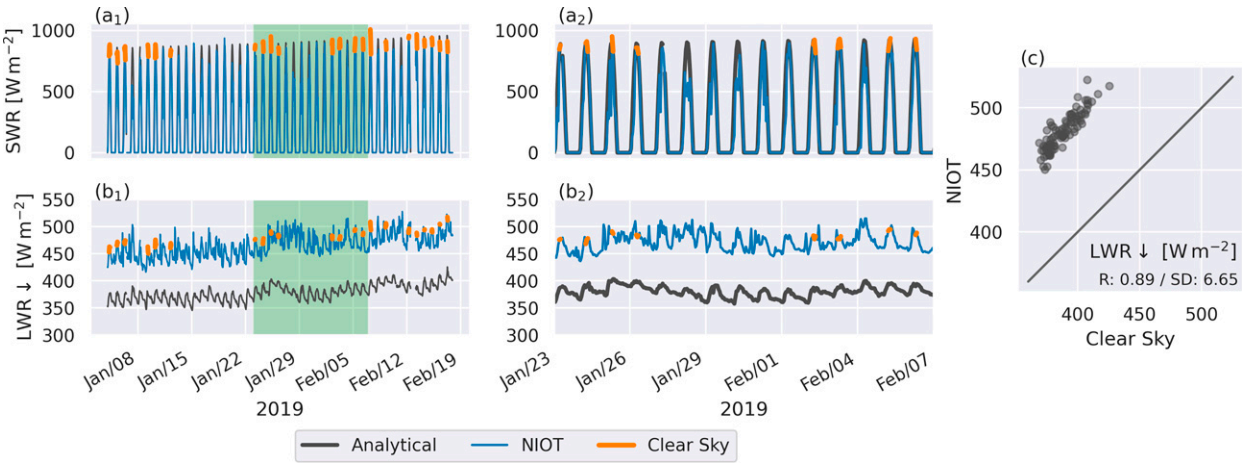

FIG. 6. Time series measurements of (a) SWR$\downarrow_{cl}$ and (b) LWR$\downarrow_{cl}$ with corresponding NIOT-OMNI measurements and (c) regression plot of theoretical LWR$\downarrow_{cl}$ Vs measured LWR$\downarrow_{cl}$, at the test station. The orange dots indicate the data points qualified as clear sky. (a2),(b2) Enhanced view of the highlighted portions of (a1) and (b1), respectively.

is the input to the amplifier, is not available for further analysis.

Because the past measurements by the OMNI moorings also need to be corrected, we therefore decided to develop a method to correct the LWR$\downarrow$ utilizing the available measurements from the OMNI buoy, which can also be applied in the field measurements. We use the theoretical values of LWR$\downarrow_{cl}$ to identify the offset value of the heat flux, which was easy to estimate using the buoy measurements of latitude, air temperature, air pressure, and relative humidity. However, the estimated LWR$\downarrow_{cl}$ exhibited a nonuniform offset with that of the measurements (since the skies are not always clear) and necessitated the identification of actual clear-sky conditions to estimate the actual offset. Therefore, the NIOT buoy measured SWR$\downarrow$ are used along with estimated SWR$\downarrow_{cl}$ to identify actual clear-sky conditions, which are used for correcting the LWR$\downarrow$. We discuss this next.

c. *Clear-sky observations*

The measured SWR$\downarrow$ values exhibited significant diurnal variability which peaks at 0600 UTC (1130 IST) and remains zero from 1300 UTC (1830 IST) to 0000 UTC (0530 IST) on every day (Fig. 6a). The daily peak varies from 552.73 W m^{-2} under cloudy conditions to 1007.81 W m^{-2} under clear conditions with most of the days recording peak values of more than 800 W m^{-2}. The daily peak values of SWR$\downarrow_{cl}$ indicated an increasing trend with the march of the seasons that varied between 858.49 W m^{-2} (on 4 January) and 958.79 W m^{-2}(on 17 February). The identification of actual clear-sky conditions is carried out by segregating the daily peaks of SWR$\downarrow$ that lies within 5% of the corresponding SWR$\downarrow_{cl}$. It is worthwhile to note that a few daily peaks of SWR$\downarrow$ values recorded more than the corresponding values of SWR$\downarrow_{cl}$ and are considered as clear-sky condition. It may be noted that most of the days (32 days) fall under the clear-sky conditions during the 45 days of the study period.

The LWR$\downarrow$ values also exhibited diurnal variability with peaks corresponding to the SWR$\downarrow$ peaks and recorded minimum values during nighttime (Fig. 6b). LWR$\downarrow$ measurements varied between 416.02 and 527.73 W m^{-2} with an average of 465.10 W m^{-2}, whereas the corresponding LWR$\downarrow_{cl}$ varied between 345.33 and 425.56 W m^{-2} with an average of 378.01 W m^{-2}. We also note that the amplitude of diurnal variability in LWR$\downarrow$ is comparatively higher than that of the LWR$\downarrow_{cl}$. It is observed that LWR$\downarrow$ values recorded sudden peaks that correspond to significantly lower daily peaks in SWR$\downarrow$ and are not accounted in clear-sky values.

The LWR$\downarrow$ values that correspond to the clear-sky conditions are segregated and carried out the 3σ test to eliminate the outliers, which resulted with a single value as outlier. The remaining observations of measured LWR$\downarrow_{cl}$ with the corresponding estimated clear-sky values exhibited a good correlation of 0.89 with a standard deviation of 6.65 W m^{-2}, which point toward the reliability of the adopted method (Fig. 6c).

d. *Correction of LWR$\downarrow$*

The offset between LWR$\downarrow$ during clear sky conditions with corresponding LWR$\downarrow_{cl}$ is estimated as 92.58 W m^{-2} and is applied in the LWR$\downarrow$ measurements during the period under study (Fig. 7). The offset corrected LWR$\downarrow$ is compared with collocated WHOI measurements to analyze the agreement between the measurements, which exhibited good correlation of 0.93 with a standard deviation of 8.3 W m^{-2} and an RMS error of 11.89 W m^{-2} after offset correction. Both the measurements exhibited similar variability such as the shift in the mean value on 24 January and higher LWR$\downarrow$ on 4 February 2019. In general, the corrected LWR$\downarrow$ is slightly higher with an average difference of −4.36 W m^{-2} than the corresponding WHOI measurements with 14.5% data recording less values.

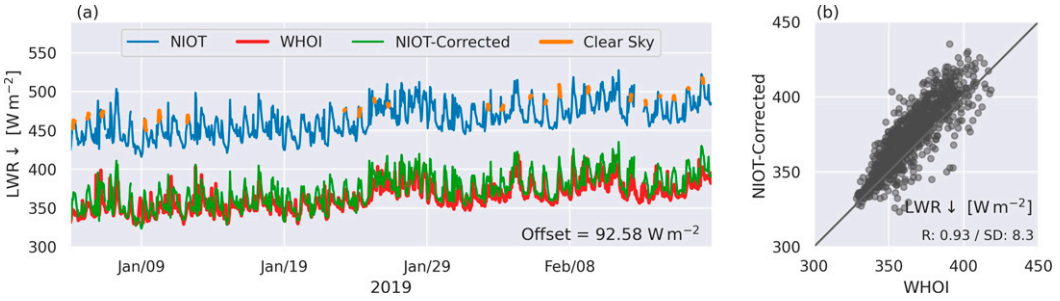

FIG. 7. The time series measurements of (a) measured and corrected LWR↓ with that of WHOI measurements and (b) regression plot of LWR↓ measurements of WHOI vs NIOT-OMNI at the NIOT test station.

e. *Correction of LWR↓ field measurements*

The OMNI buoy BD09 located in north BoB has been operational since March 2013. As part of the air–sea interaction collaboration between the United States and India (Wijesekera et al. 2016), the WHOI deployed an air–sea flux mooring 27 km away from BD09 in December 2014 and continued the measurements until January 2016. Both the buoys were fitted with a suite of meteorological and oceanographic sensors including LWR↓ and SWR↓ sensors.

The seasonal variability is well depicted in the time series observations, which is reported in detail by Weller et al. (2019). Intercomparison of air temperature, air pressure, relative humidity, and SST exhibited similar trend and good agreement with a correlation of more than 0.95 (Figs. 8b–e). However, the OMNI measured LWR↓ exhibited an overestimation and large scatter compared to that of WHOI measurements even though the trend appears to be the same (Fig. 8a). The quality control of the LWR↓ is carried out by replacing the 0 values and the spikes in voltage measurements using the 2-min measurements and recomputing the LWR↓ values.

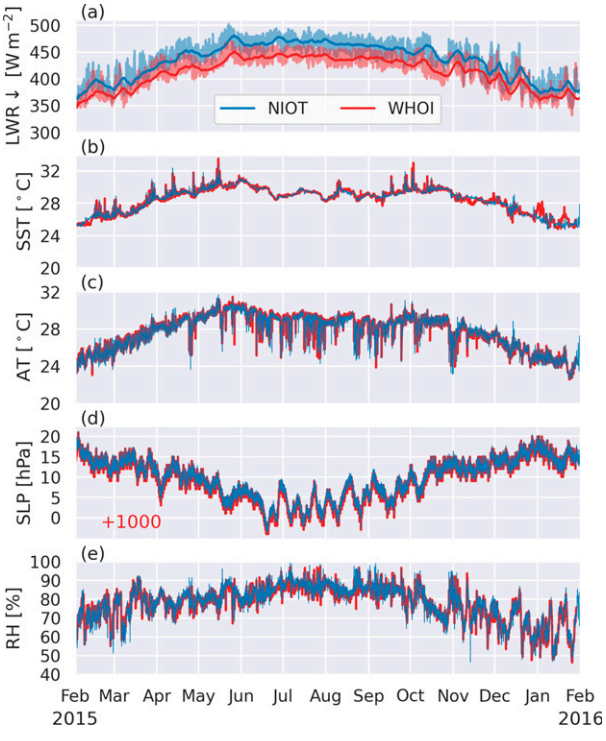

FIG. 8. Time series observations of NIOT OMNI buoy (blue) and WHOI buoy (red): (a) LWR↓, (b) SST, (c) air temperature, (d) air pressure, and (e) relative humidity. The thin lines in (a) represent the hourly measurements whereas the corresponding thick lines represent the weekly moving average.

The measured as well as the estimated values of SWR$\downarrow_{cl}$ exhibited significant seasonal variability with more than 1000 W m^{-2} during summer and a minimum of ~800 W m^{-2} during winter (Fig. 9). The analysis revealed mostly clear sky, which recorded more than the estimated SWR$\downarrow_{cl}$ during February to early March. SWR↓ values during May–August 2015 were much less than the estimated SWR$\downarrow_{cl}$ indicating the cloudy conditions during the southwest monsoon. The remaining period recorded intermittent clear sky occasionally exceeding the estimated SWR$\downarrow_{cl}$.

The LWR↓ exhibits seasonal variability with maximum values recorded during May to September 2015, owing to the cloudy conditions during southwest monsoon, which is also reflected in the estimated LWR$\downarrow_{cl}$. The LWR$\downarrow_{cl}$ exhibits larger deviation from the measured LWR↓ during the southwest monsoon compared to the remaining period, which is also observed at WHOI location. However, the estimated LWR$\downarrow_{cl}$ at WHOI location is in the same range as that of LWR↓ measurements with an offset of 2.91 W m^{-2}.

For calculating the effective emissivity, we used both the two-parameter fit by Brunt (1932) and the three-parameter fit [Eq. (3)] by Fairall et al. (2008). The estimation of effective emissivity for clear sky using the three-parameter fit by Fairall et al. (2008) exhibited less deviation during the southwest monsoon compared to that of the two-parameter fit by Brunt (1932). This suggests the importance of the total precipitable water in the atmosphere in estimating the LWR$\downarrow_{cl}$. However, the application of the coefficients estimated based on the measurements from eastern equatorial Pacific Ocean without any adjustments in the latitude dependence may have resulted in the comparatively lower values during the southwest monsoon season.

Our analysis revealed 102 LWR↓ measurements that correspond to clear-sky conditions over the period of one year with a correlation of 0.94 and a standard deviation of 10.99 W m^{-2}

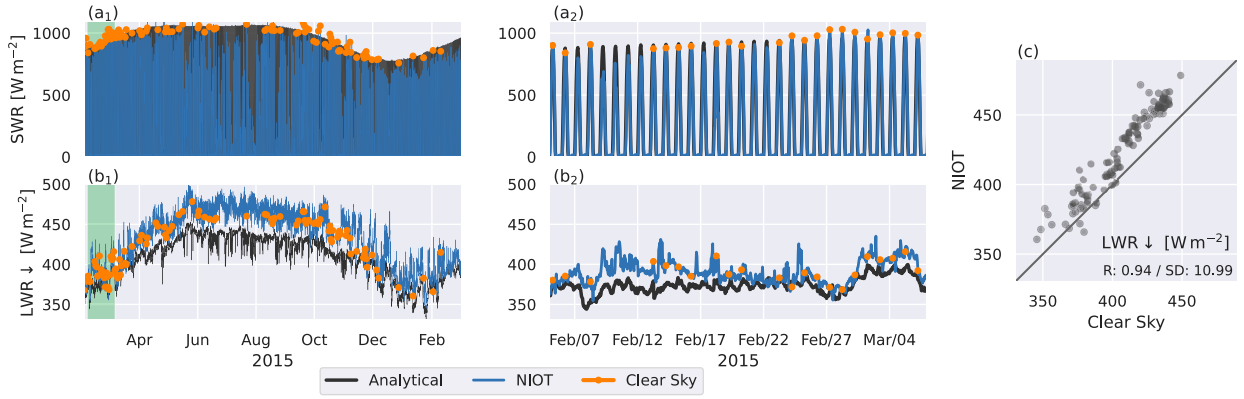

FIG. 9. The intercomparison of measured and estimated clear-sky values of (a) SWR↓ and (b) LWR↓ along with clear-sky conditions (orange dots) and (c) the regression plot of theoretical $LWR\downarrow_{cl}$ vs measured $LWR\downarrow_{cl}$ in the north BoB; (a2),(b2) Enhanced view of the highlighted portions of (a1) and (b1), respectively.

(Fig. 9). This point toward the reliability of the method, and hence the offset of 19.22 W m^{-2} is applied in measured LWR↓.

The intercomparison of corrected LWR↓ with the nearby WHOI measurements exhibits a correlation of 0.95 with a standard deviation of 10.85 W m^{-2} and RMS error of 8.89 W m^{-2} (Fig. 10). The corrected NIOT OMNI LWR↓ exhibits higher values (average difference of 3.46 W m^{-2}) than that of WHOI particularly during April–October 2015. The presence of local clouds during the southwest monsoon could be a reason for the difference in these measurements. It also points toward the necessity for deriving the local coefficients for better estimating the emissivity to further improve the results.

4. Summary

The analysis of LWR↓ measurements at the test station at NIOT and at the OMNI buoy BD09 in north BoB revealed significant offsets, which varied with each deployment. It necessitates the estimation of the offset during each deployment to correct the past data. In general, the LWR↓ values are overestimated and the study revealed an offset of 92.58 W m^{-2} at test station whereas that of BD09 in north BoB is only 19.22 W m^{-2}. In both the experiments, the corrected values are in good agreement with that of the collocated WHOI measurements, which indicates the reliability of the method. We further note that $LWR\downarrow_{cl}$ strongly depends on the presence of Integrated water vapor in the atmosphere. The estimation of the coefficients for emissivity from the measurements in the north Indian Ocean will provide better picture of the variability particularly during the southwest monsoon season.

The proposed method can be easily applied in correcting the past OMNI LWR↓ measurements and offers a value addition in surface meteorological observations as well as air–sea flux studies. The overestimation of LWR↓ measurements due to the malfunctioning of the gain amplifier emphasizes the importance of regular calibration of thermopile amplifier to ensure stable amplification of microvolt signals. Improved LWR↓ measurements can be achieved with a dedicated sensor module comprising signal processing electronics with stable amplification and datalogger capable of processing the microvolt signals. Following this study, this recommendation has been incorporated in OMNI buoys, and going forward, the OMNI setup now utilizes the

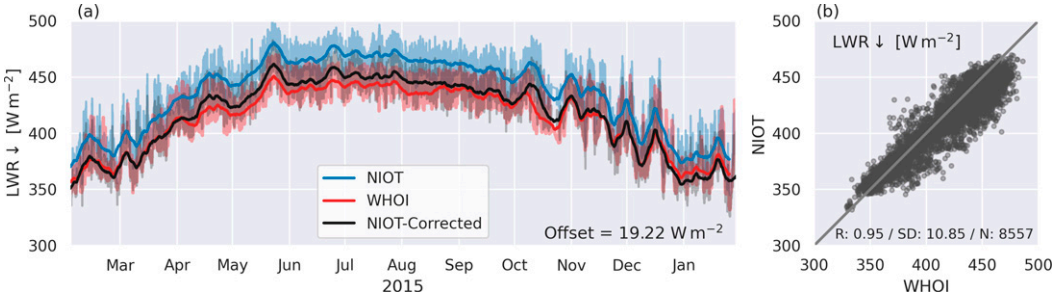

FIG.10. The time series measurements of (a) measured and corrected LWR↓ with that of WHOI measurements and (b) regression plot of LWR↓ measurements of WHOI vs NIOT-OMNI in the north BoB during February 2015–January 2016. The thin lines represent the hourly measurements, whereas the corresponding thick lines represent the weekly moving averages.

WHOI sensor module with stable amplification and signal processing electronics for LWR↓ measurements.

Acknowledgments. KJJ and RV thank Ministry of Earth Sciences (MoES), Government of India, Secretary, MoES, and Director, NIOT, for the support and encouragement in carrying out the work under the National Monsoon Mission, Ocean Mixing and Monsoon (OMM) program. AT, JTF, and RAW thank Office of Naval Research Grants N00014-19-12410 and N00014-17-12880, United States, for funding and support. The OOS team at NIOT is acknowledged for their efforts in maintaining the OMNI buoy network in North Indian Ocean. We acknowledge Dr. B.W. Blomquist, University of Colorado, for his support in computing clear-sky radiation and Iury T. Simoes-Sousa, University of Massachusetts, Dartmouth, for the graphics. NCMRWF, MoES, Government of India, is acknowledged for NGFS reanalysis dataset, which is produced under the collaboration between NCMRWF, IITM, and IMD.

Data availability statement. The dataset utilized in field validation are available for the public. The OMNI data are available at http://do.incois.gov.in/ and the WHOI data are available at http://uop.whoi.edu/projects/Bengal/QCData.html.

REFERENCES

Albrecht, B., and S. K. Cox, 1977: Procedures for improving pyrgeometer performance. *J. Appl. Meteor.*, **16**, 188–197, https://doi.org/10.1175/1520-0450(1977)016<0190:PFIPP>2.0.CO;2.

Bhat, G. S., 2003: Near surface variations and surface fluxes over the northern Bay of Bengal during the 1999 Indian summer monsoon. *J. Geophys. Res.*, **107**, 4336, https://doi.org/10.1029/2001JD000382.

——, and C. P. Chandrasekhar, 2001: The Bay of Bengal Monsoon Experiment: BOBMEX. ORV Sagar Kanya radiosonde profiles. Indian Institute of Science Centre for Atmospheric Oceanic Sciences Rep. ICRP/IISC/CAOS/02, 200 pp.

——, S. Ameenulla, M. Venkataramana, and K. Sengupta, 2000: Atmospheric boundary layer characteristics during the BOBMEX-Pilot experiment. *J. Earth Syst. Sci.*, **109**, 229–237, https://doi.org/10.1007/BF02702196.

——, and Coauthors, 2001: BOBMEX—The Bay of Bengal Monsoon Experiment. *Bull. Amer. Meteor. Soc.*, **82**, 2217–2243, https://doi.org/10.1175/1520-0477(2001)082<2217:BTBOBM>2.3.CO;2.

Brunt, D., 1932: Notes on radiation in the atmosphere. *Quart. J. Roy. Meteor. Soc.*, **58**, 389–420, https://doi.org/10.1002/qj.49705824704.

Dickey, T. D., D. V. Mano, D. A. Siegel, and R. A. Weller, 1994: Determination of longwave heat flux at the air–sea interface using measurements from buoy platforms. *J. Atmos. Oceanic Technol.*, **11**, 1057–1078, https://doi.org/10.1175/1520-0426(1994)011<1057:DOLHFA>2.0.CO;2.

Enz, J. W., J. C. Klink, and D. G. Baker, 1975: Solar radiation effects on pyrgeometer performance. *J. Appl. Meteor. Climatol.*, **14**, 1297–1302, https://doi.org/10.1175/1520-0450(1975)014<1297:SREOPP>2.0.CO;2.

EPLAB, 2016: Precision Infrared Radiometer. EPLAB Doc., 1 p., http://www.eppleylab.com/wp-content/uploads/pdf/EPPLEY160919-PIR.pdf.

Fairall, C. W., E. F. Bradley, D. P. Rogers, J. B. Edson, and G. S. Young, 1996: Bulk parameterization of air-sea fluxes for Tropical Ocean-Global Atmosphere Coupled-Ocean Atmosphere Response Experiment. *J. Geophys. Res.*, **101**, 3747–3764, https://doi.org/10.1029/95JC03205.

——, T. Uttal, D. Hazen, J. Hare, M. F. Cronin, N. Bond, and D. E. Veron, 2008: Observations of cloud, radiation, and surface forcing in the equatorial eastern Pacific. *J. Climate*, **21**, 655–673, https://doi.org/10.1175/2007JCLI1757.1.

Foltz, G. R., J. Vialard, B. P. Kumar, and M. J. McPhaden, 2010: Seasonal mixed layer heat balance of the southwestern tropical Indian Ocean. *J. Climate*, **23**, 947–965, https://doi.org/10.1175/2009JCLI3268.1.

Fugro OCEANOR, 2012: SW06 SEAWATCH Wavescan Buoy. Fugro OCEANOR Doc., 4 pp., https://metrica-env.gr/images/Downloads/brochures/oceanografika/SW06_SEAWATCH_Wavescan_Buoy_FINAL.pdf.

Hastenrath, S., and P. J. Lamb, 1979: *Climatic Atlas of the Indian Ocean—Part I: Surface Climate and Atmospheric Circulation*. University of Wisconsin Press, 109 pp.

Hosom, D. S., R. A. Weller, R. E. Payne, and K. E. Prada, 1995: The IMET (improved meteorology) ship and buoy system. *J. Atmos. Oceanic Technol.*, **12**, 527–540, https://doi.org/10.1175/1520-0426(1995)012<0527:TIMSAB>2.0.CO;2.

Iqbal, M., 1988: Spectral and total sun radiance under cloudless skies. *Physical Climatology for Solar and Wind Energy*, R. Guzzi and C. G. Justus, Eds., World Scientific, 196–242.

Jones, C. S., D. M. Legler, and J. J. O'Brien, 1995: Variability of surface fluxes over the Indian Ocean; 1960–1989. *Global Atmos. Ocean Syst.*, **3**, 249–272.

Kiehl, J. T., and K. E Trenberth. 1997: Earth's annual global mean energy budget. *Bull. Amer. Meteor. Soc.*, **78**, 197–208, https://doi.org/10.1175/1520-0477(1997)078%3C0197:EAGMEB%3E2.0.CO;2.

King, M. D., Y. J. Kaufman, W. P. Menzel, and D. Tanré, 1992: Remote sensing of cloud, aerosol, and water vapor properties from the Moderate Resolution Imaging Spectrometer (MODIS). *IEEE Trans. Geosci. Remote Sens.*, **30**, 2–27, https://doi.org/10.1109/36.124212.

Kumar, R., S. Chaudhury, S. K. Peshin, S. K. Srivastava, T. K. Mandal, and A. P. Mitra, 2001: First time observation of latitudinal and vertical distribution of infra-red radiative flux using radiometer sonde over Indian Ocean during the INDOEX IFP-1999 and its comparison with other Indian stations. *Curr. Sci.*, **80**, 209–215.

Marty, C., 2000: Surface radiation, cloud forcing and greenhouse effect in the Alps. Ph.D. dissertation, ETH Zurich, 140 pp.

——, and R. Philipona, 2000: The clear-sky index to separate clear-sky from cloudy-sky situations in climate research. *Geophys. Res. Lett.*, **27**, 2649–2652, https://doi.org/10.1029/2000GL011743.

McPhaden, M. J., and G. R. Foltz, 2013: Intraseasonal variations in the surface layer heat balance of the central equatorial Indian Ocean: The importance of zonal advection and vertical mixing. *Geophys. Res. Lett.*, **40**, 2737–2741, https://doi.org/10.1002/grl.50536.

Ohmura, A., and Coauthors, 1998: Baseline Surface Radiation Network (BSRN/WCRP): New precision radiometry for climate research. *Bull. Amer. Meteor. Soc.*, **79**, 2115–2136, https://doi.org/10.1175/1520-0477(1998)079<2115:BSRNBW>2.0.CO;2.

Payne, R. E., and S. P. Anderson, 1999: A new look at calibration and use of Eppley Precision Infrared Radiometers. Part II: Calibration and use of the Woods Hole Oceanographic

Institution Improved Meteorology Precision Infrared Radiometer. *J. Atmos. Oceanic Technol.*, **16**, 739–751, https://doi.org/10.1175/1520-0426(1999)016<0739:ANLACA>2.0.CO;2.

Philipona, R., C. Frohlich, and Ch. Betz, 1995: Characterization of pyrgeometers and the accuracy of atmospheric long-wave radiation measurements. *Appl. Opt.*, **34**, 1598–1605, https://doi.org/10.1364/AO.34.001598.

——, C. Marty, C. Fröhlich, and A. Heimo, 1996: Measurements of the longwave radiation budget in the Alps. *Proc. Int. Radiation Symp.*, Fairbanks, AK, IRS, 786–789.

——, and Coauthors, 1998: The Baseline Surface Radiation Network pyrgeometer round-robin calibration experiment. *J. Atmos. Oceanic Technol.*, **15**, 687–696, https://doi.org/10.1175/1520-0426(1998)015<0687:TBSRNP>2.0.CO;2.

——, and Coauthors, 2001: Atmospheric longwave irradiance uncertainty: Pyrgeometers compared to an absolute sky-scanning radiometer, atmospheric emitted radiance interferometer, and radiative transfer model calculations. *J. Geophys. Res.*, **106**, 28 129–28 141, https://doi.org/10.1029/2000JD000196.

Pinker, R. T., H. Wang, and S. A. Grodsky, 2009: How good are ocean buoy observations of radiative fluxes? *Geophys. Res. Lett.*, **36**, L10811, https://doi.org/10.1029/2009GL037840.

——, A. Bentamy, K. B. Katsaros, Y. Ma, and C. Li, 2014: Estimates of net heat fluxes over the Atlantic Ocean. *J. Geophys. Res. Oceans*, **119**, 410–427, https://doi.org/10.1002/2013JC009386.

——, B. Zhang, R. A. Weller, and W. Chen, 2018: Evaluating surface radiation fluxes observed from satellites in the southeastern Pacific Ocean. *Geophys. Res. Lett.*, **45**, 2404–2412, https://doi.org/10.1002/2017GL076805.

Prasad, V. S., S. Mohandas, M. D. Gupta, E. N. Rajagopal, and S. K. Dutta, 2011: Implementation of upgraded global forecasting systems (T382L64 and T574L64) at NCMRWF. NCMRWF Tech. Rep. NCMR/TR/5/2011, 72 pp.

——, C. J. Johny, P. Mali, S. K. Singh, and E. N. Rajagopal, 2017: Global retrospective analysis of NGFS for the period 2000–2011. *Curr. Sci.*, **112**, 370–377, https://doi.org/10.18520/cs/v112/i02/370-377.

Premkumar, K., M. Ravichandran, S. Kalsi, D. Sengupta, and S. Gadgil, 2000: First results from a new observational system over the Indian seas. *Curr. Sci.*, **78**, 323–330.

Rajeevan, M., P. Rohini, K. N. Kumar, J. Srinivasan, and C. K. Unnikrishnan, 2013: A study of vertical cloud structure of the Indian summer monsoon using CloudSat data. *Climate Dyn.*, **40**, 637–650, https://doi.org/10.1007/s00382-012-1374-4.

Ramanathan V., R. D. Cess, E. F. Harrison, P. Minnis, B. R. Barkstrom, E. Ahmad, and D. Hartmann, 1989: Cloud-radiative forcing and climate: Results from the Earth Radiation Budget Experiment. *Science*, **243**, 57–63, https://doi.org/10.1126/science.243.4887.57.

Ramesh Kumar, M. R., R. T. Pinker, S. Mathew, R. Venkatesan, and W. Chen, 2017: Evaluation of radiative fluxes over the north Indian Ocean. *Theor. Appl. Climatol.*, **132**, 983–988, https://doi.org/10.1007/s00704-017-2141-6.

Rossow, W. B., and R. A. Schiffer, 1999: Advances in understanding clouds from ISCCP. *Bull. Amer. Meteor. Soc.*, **80**, 2261–2287, https://doi.org/10.1175/1520-0477(1999)080<2261:AIUCFI>2.0.CO;2.

Sengupta, D., S. R. Parampil, G. S. Bhat, V. S. N. Murty, V. Ramesh Babu, T. Sudhakar, K. Premkumar, and Y. Pradhan, 2008: Warm pool thermodynamics from the Arabian Sea Monsoon Experiment (ARMEX). *J. Geophys. Res.*, **113**, C10008, https://doi.org/10.1029/2007JC004623.

Thandlam, V., and H. Rahaman, 2019: Evaluation of surface shortwave and longwave downwelling radiations over the global tropical oceans. *SN Appl. Sci.*, **1**, 1171, https://doi.org/10.1007/s42452-019-1172-2.

Tomita, H., and M. Kubota, 2004: Variability of surface heat flux over the Indian Ocean. *Atmos.–Ocean*, **42**, 183–199, https://doi.org/10.3137/ao.420303.

Venkatesan, R., V. R. Shamji, G. Latha, S. Mathew, R. R. Rao, A. Muthiah, and M. A. Atmanand, 2013: In situ ocean subsurface time-series measurements from OMNI buoy network in the Bay of Bengal. *Curr. Sci.*, **104**, 1166–1177.

Venugopal, T., H. Rahaman, M. Ravichandran, and S. S. V. S. Ramakrishna, 2016: Evaluation of MODIS/CERES downwelling shortwave and longwave radiation over global tropical oceans. *Proc. SPIE*, **9876**, 98761F, https://doi.org/10.1117/12.2228041.

Webster, P. J., and Coauthors, 2002: The JASMINE pilot study. *Bull. Amer. Meteor. Soc.*, **83**, 1603–1630, https://doi.org/10.1175/BAMS-83-11-1603.

Weller, R. A., 2006: Surface radiation observations in the open ocean. WHOI Tech. Note TN-June06, 2 pp.

——, 2018: Observing surface meteorology and air-sea fluxes. *Observing the Oceans in Real Time*, R. Venkatesan et al., Eds., Springer Oceanography, Springer, 17–36.

——, and S. P. Anderson, 1996: Surface meteorology and air–sea fluxes in the western equatorial Pacific warm pool during the TOGA Coupled Ocean–Atmosphere Response Experiment. *J. Climate*, **9**, 1959–1990, https://doi.org/10.1175/1520-0442(1996)009<1959:SMAASF>2.0.CO;2.

——, S. P. Bigorre, J. Lord, J. D. Ware, and J. B. Edson, 2012: A surface mooring for air–sea interaction research in the Gulf Stream. Part I: Mooring design and instrumentation. *J. Atmos. Oceanic Technol.*, **29**, 1363–1376, https://doi.org/10.1175/JTECH-D-12-00060.1.

——, J. T. Farrar, H. Seo, C. Prend, D. Sengupta, J. S. Lekha, M. Ravichandran, and R. Venkatesen, 2019: Moored observations of the surface meteorology and air–sea fluxes in the northern Bay of Bengal in 2015. *J. Climate*, **32**, 549–573, https://doi.org/10.1175/JCLI-D-18-0413.1.

——, ——, S. Bigorre, J. Smith, J. Potemra, and F. Santiago-Mandujano, 2020: Best practices for surface radiation observations from long-term moored buoys. *EGU General Assembly*, Online, 2025, https://presentations.copernicus.org/EGU2020/EGU2020-2025_presentation.pdf.

Wijesekera, H. W., and Coauthors, 2016: ASIRI: An ocean–atmosphere initiative for Bay of Bengal. *Bull. Amer. Meteor. Soc.*, **97**, 1859–1884, https://doi.org/10.1175/BAMS-D-14-00197.1.

Zeng, X., M. Zhao, and R. E. Dickinson, 1998: Intercomparison of bulk aerodynamic algorithms for computation of sea surface fluxes using TOGA COARE and TAO data. *J. Climate*, **11**, 2628–2644, https://doi.org/10.1175/1520-0442(1998)011<2628:IOBAAF>2.0.CO;2.